

Anisotropic Tetratellurium-Iridium-Niobium terahertz detector

LIU Yuan^{1,2}, XU Yong-Jiang^{1,2}, LAI Zhi-Hong^{1,2}, SHEN Yun^{1*}, YANG Si-Jia^{2*}, DENG Xiao-Hua^{2*}

(1. School of Physics and Materials, Nanchang University, Nanchang 330031, China;
2. Institute of Space Science and Technology, Nanchang University, Nanchang 330031, China)

Abstract: Topological semimetal materials have garnered significant interest due to their distinctive electronic structures and unique properties. They serve as a foundation for exploring various physical phenomena including the anomalous Hall effect, topological phase transitions and negative magnetoresistance, while also offering potential solutions to the "THz Gap." This study focuses on the type-II Weyl semimetal tetratellurium iridium niobium (NbIrTe_4) terahertz detector which exhibits a responsivity of 4.36 A/W, a noise equivalent power of 12.34 pW/Hz^{1/2} and an anisotropic resistance ratio of 32 at room temperature. This research paves the way for achieving high-performance terahertz detection at room temperature and serves as a reference for investigating the Weyl semimetal.

Key words: semimetal, terahertz, detector, anisotropy

具有各向异性的四碲铱铌太赫兹探测器

刘远^{1,2}, 许永姜^{1,2}, 赖志鸿^{1,2}, 沈云^{1*}, 杨思嘉^{2*}, 邓晓华^{2*}

(1. 南昌大学物理与材料学院,江西南昌330031;
2. 南昌大学空间科学与技术研究院,江西南昌330031)

摘要:拓扑半金属材料由于其独特的电子结构和非平凡特性受到了广泛的关注,不仅为反常霍尔效应、拓扑相变和负磁阻等物理现象的研究提供了土壤,同时为突破“THz Gap”提供了机会。本文基于Ⅱ型外尔半金属四碲铱铌(NbIrTe_4)的太赫兹探测器在室温下具有4.36 A/W的响应度,12.34 pW/Hz^{1/2}的噪声等效功率和32的各向异性电阻比。研究为室温下实现高效的太赫兹探测提供了一种思路,同时为外尔半金属的研究提供了一些参考。

关 键 词:半金属;太赫兹;探测器;各向异性

中图分类号:O439

文献标识码:A

Introduction

Terahertz technology is an advanced research area that combines electronics and photonics with numerous applications such as image analysis, rapid imaging, gene analysis, biosensing, agricultural monitoring and 6G communications^[1-9]. However, the terahertz frequency range is often referred to as the "THz Gap" in the electromagnetic spectrum due to the absence of efficient room-temperature terahertz sources and detectors. This presents a significant challenge in creating terahertz detectors that are highly responsive, low-noise, sensitive and energy-efficient. While various types of detectors have been

developed, including Golay^[10], pyroelectric^[11-12] and bolometer detectors^[13-17], issues related to low response, low sensitivity and the requirement for low temperatures remain unresolved.

Topological semimetals are promising materials for developing high-performance photodetectors, exhibiting features such as chiral anomalies, nonlinear photoresponse, negative magnetoresistance and nonlinear Hall effects^[18-22]. These materials are categorized into Dirac semimetals, Weyl semimetals and nodal-line semimetals (NLS). Dirac semimetals possess remarkable topological properties with their conduction and valence bands inter-

Received date: 2024-12-13, revised date: 2025-01-29

收稿日期:2024-12-13,修回日期:2025-01-29

Foundation items: Supported by the National Natural Science Foundation of China (61865009); National Natural Science Foundation of China Major Research Equipment Development Project (61927813)

Biography: LIU Yuan (1997-), male, JiangXi, Master. Research area involves terahertz detector. E-mail: yuanliu249@163. com.

* Corresponding authors: E-mail: Dengxiaohua0@gmail. com, 1174904727@qq. com, shenyun@ncu. edu. com

secting at the Dirac point near the Fermi level, resulting in massless carrier-fermions that exhibit linear dispersion across all momentum directions^[23]. Nodal-line semimetals, on the other hand, have linearly dispersed band intersections that form closed loops in the Brillouin zone, showcasing unique quantum properties such as ultra-low thermal conductivity, exceptional stability, the quantum Hall effect and giant magnetoresistance^[24-25].

When inversion symmetry is disrupted, Dirac semimetals transition into Weyl semimetals. Weyl semimetals can be further classified into type-I and type-II based on the characteristics of the Weyl cone. Type-II Weyl semimetals exhibit significant Berry curvature near their tilted Weyl cone^[26-28]. Although the existence of type-II Weyl points and the unique surface states and Fermi arcs of NbIrTe₄ have been confirmed through density functional theory and angle-resolved photoelectron spectroscopy, reports on high-performance terahertz detectors made from type-II Weyl semimetal NbIrTe₄ are scarce^[29].

In this study, the band structure and surface states of NbIrTe₄ were analyzed using the first-principles software Wannier90. The calculated Weyl point is located close to the Fermi level which enhances carrier transport and makes it suitable for developing high-performance terahertz detectors. Subsequently, a metal-NbIrTe₄-metal field-effect transistor was fabricated using micro-nano processing techniques and its electrical characteristics and terahertz photocurrent response were evaluated. The findings indicate that the NbIrTe₄-based terahertz detector exhibits a wide linear dynamic range and excellent stability in air. The responsivity at room temperature is 4.36 A/W with a noise equivalent power of approximately 12.34 pW/Hz^{1/2}. Even at zero bias, the responsivity remains at 1.38A/W while the noise equivalent power decreases to 4.65 pW/Hz^{1/2}. Lastly, to investigate the mate-

rial's anisotropy, an eight-electrode structure was created, revealing an anisotropic resistance ratio of 32.

1 First principles calculations

The space group of NbIrTe₄ is Pmn2₁. The crystal is non-centrosymmetric and orthorhombic and its structure is shown in Figure 1a, 1b. The lattice constants of this material are significantly different. The x-axis length is 3.768 Å, the y-axis is 12.486 Å and the z-axis is 13.077 Å. The obvious length difference between the x-axis and the y-axis gives NbIrTe₄ an in-plane strong anisotropy.

The first-principles calculation software Wannier90 was utilized to analyze the NbIrTe₄ material, incorporating the effects of spin-orbit coupling (SOC). In the energy band structure diagram presented in Figure 2a, the tilted Weyl cone of NbIrTe₄ and the Weyl point close to the Fermi surface are clearly visible, which facilitates the transition of carrier energy bands under low-frequency terahertz photon radiation, leading to the generation of light current. Additionally, an analysis of its energy band structure with respect to atomic orbital characteristics presented in Figure 2b revealed multiple instances of energy band inversion between the p orbitals of Te and the d orbitals of Nb near the Γ point, further confirming the topological nature of NbIrTe₄. Furthermore, it was noted that the energy bands near the Fermi surface are significantly influenced by the 5d orbitals of Nb, the 5p orbitals of Te and the 5d orbitals of Ir, aligning with the calculated results of the corresponding partial wave density of states. The calculation results for the (001) surface state of NbIrTe₄, illustrated in Figure 2c, indicate distinct differences between the bulk and surface states in certain energy bands^[29]. Notably, several key features

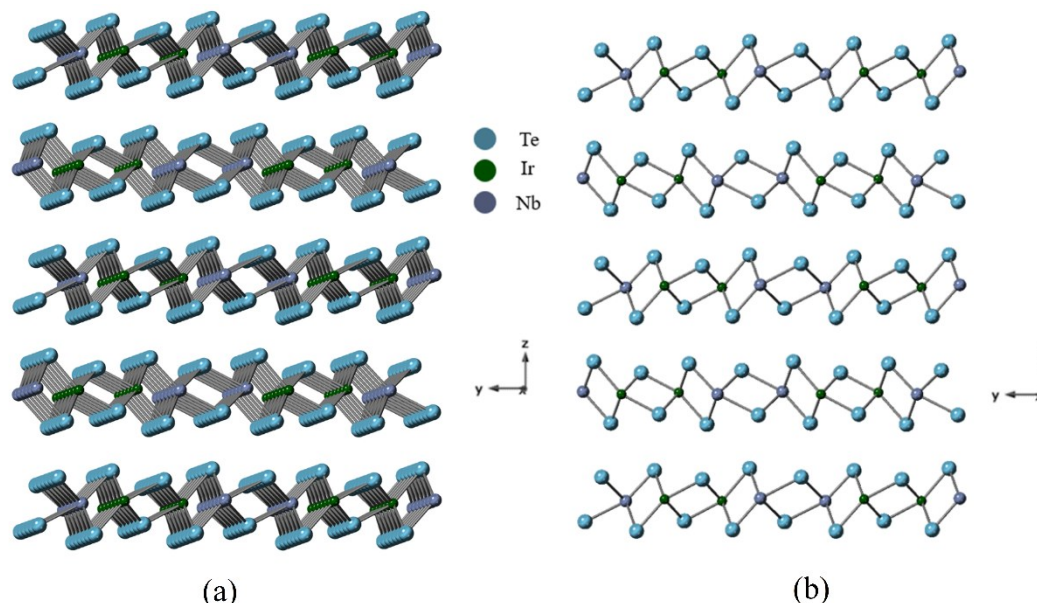


Fig. 1 Crystal structure of NbIrTe₄. (a), (b) 3D image and xy plane projection of NbIrTe₄. The blue ones are Te atoms, the green ones are Ir atoms and the purple ones are Nb atoms.

图1 NbIrTe₄的晶体结构。(a), (b) NbIrTe₄的三维立体图和xy平面投影。蓝色的是Te原子,绿色是Ir原子和紫色的Nb原子。

were identified: an elliptical hole pocket (labeled BVB) on the Fermi surface along the Γ -X direction, which signifies the contribution from the bulk material. Additionally, hourglass-like features around Γ and eye-like features around Y (marked as SS) were observed, with these shapes primarily contributing to the surface. Moreover, an arc near the elliptical hole pocket corresponds to the Fermi Arc position (labeled SA), which evolves from the Fermi arc state at the Weyl point.

2 Results and discussion

NbIrTe_4 material comes from Professor Sun Cun-zhi of Xiamen University. X-ray diffraction (XRD) measurement was performed on NbIrTe_4 material and the results are shown in Figure 3a. It can be seen that there are very high peaks and narrow half-wave widths, and there are almost no impurity peaks indicating that the material has high crystallinity. In addition, Raman characterization was performed using a laser confocal Raman spectrometer and the results are shown in Figure 3b. It can be seen that the vibration peak of the material appears at 193cm^{-1} , corresponding to the E_g vibration peak.

The planar antenna captures terahertz photons, leading to the creation of pseudo-plasma oscillations that increase the electric field strength at both ends of the material. This enhancement facilitates the directional movement of carriers, resulting in the generation of photocurrent [30]. This study employs FDTD electromagnetic software to simulate and optimize a half-wave dipole logarithmic periodic antenna. For composite light radiation ranging from 0.1 to 1 THz, the antenna's radius ratio is fine-tuned to achieve the optimal structure. As illustrated in Figure 4a, the antenna's channel width measures 4 mm, which is narrower than the terahertz spot size. Following optimization, the radius ratio (R_n/r_n) is determined to be 1.76, at which point the antenna structure maximally absorbs terahertz photons, and the electric field strength at both ends of the channel is at its peak. Figure 4b depicts the electrode structure post-metal evaporation.

The detector is constructed as a metal- NbIrTe_4 -metal field effect transistor utilizing micro-nano processing technology to enable better integration of the device, promoting miniaturization and industrial application as illustrated in Figure 5a. The primary steps in the process in-

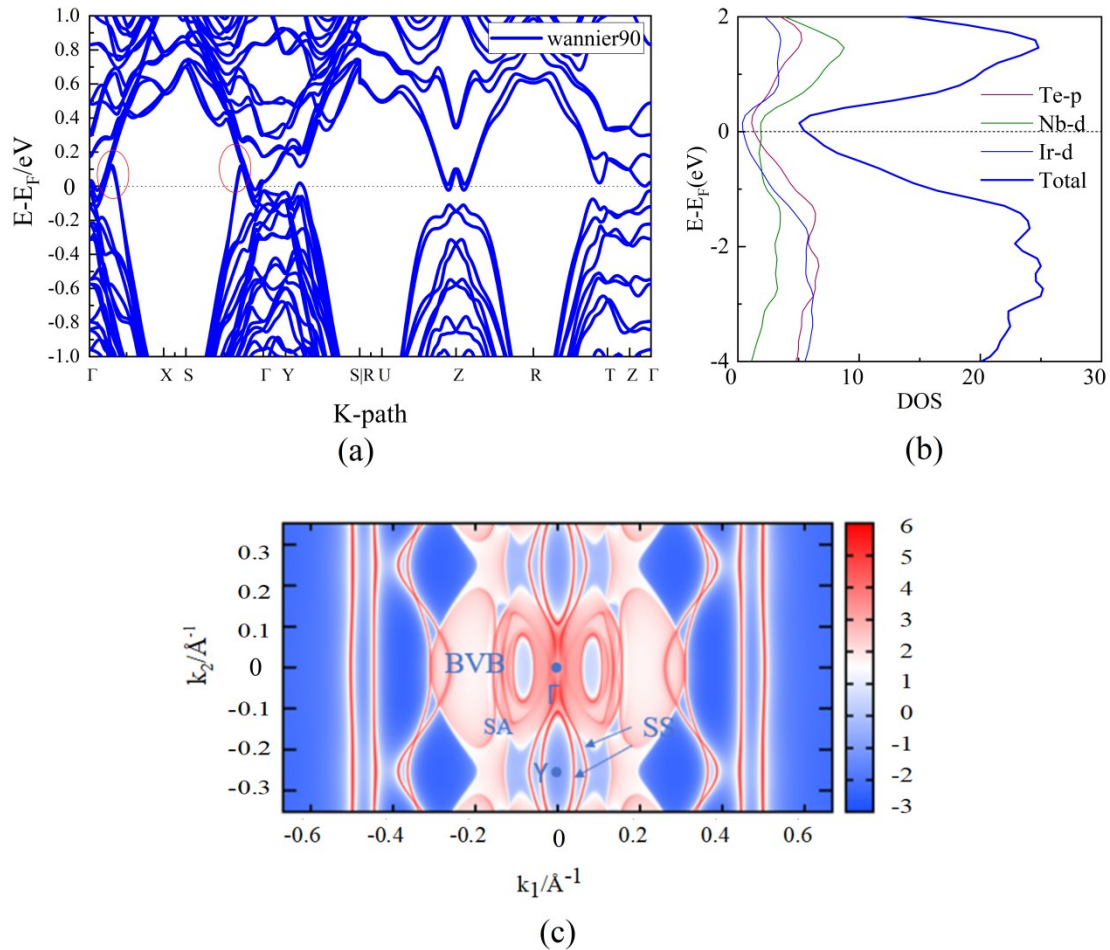


Fig. 2 Calculated band structure and surface states of NbIrTe_4 : (a) Band structure of NbIrTe_4 . The red circles indicate the Weyl points of the material. The dotted line indicates the Fermi surface; (b) Density of states of NbIrTe_4 ; (c) Calculated Fermi arc of NbIrTe_4 on the (001) surface

图2 计算出的 NbIrTe_4 的能带结构和表面态:(a) NbIrTe_4 的能带结构, 红色圆圈标注出来的是材料的外尔点, 虚线表示的是费米面;(b) NbIrTe_4 的态密度;(c) NbIrTe_4 在(001)面的费米弧计算结果

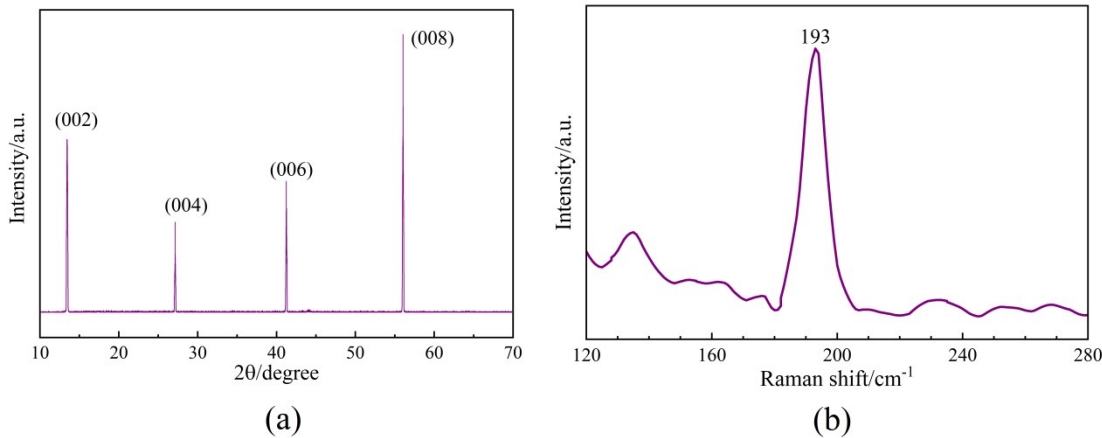


Fig. 3 Characterization of NbIrTe_4 : (a) XRD characterization of NbIrTe_4 with high peaks, narrow half-wave width and almost no impurity peaks. The inset is a well-grown NbIrTe_4 crystal; (b) Raman characterization of NbIrTe_4 . The inset is a NbIrTe_4 crystal photographed with a microscope.

图3 (a) NbIrTe_4 的XRD表征, 波峰高, 半波宽窄并且几乎没有杂峰。插图是生长好的 NbIrTe_4 晶体;(b) NbIrTe_4 的拉曼表征。插图是用显微镜拍摄的 NbIrTe_4 晶体

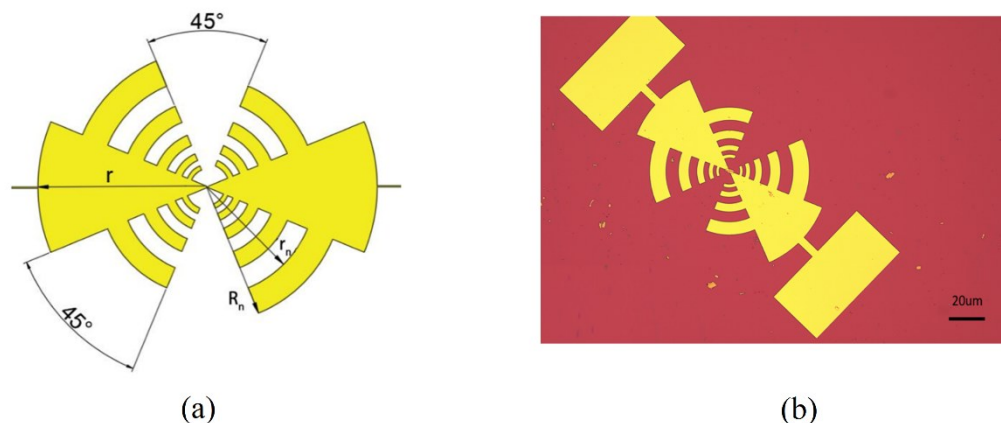


Fig. 4 Schematic diagram of the antenna structure of the device: (a) The shape of the logarithmic periodic antenna. (b) The logarithmic periodic antenna structure that has been plated with metal

图4 器件的天线结构和测量示意图:(a) 已经镀好金属的对数周期天线结构;(b) FDTD 仿真优化后的局部电场强度

clude: transferring the NbIrTe_4 material onto a clean substrate using a two-dimensional transfer platform, employing a laser direct writing tool for photolithography of the antenna structure, evaporating a metal plating layer at high temperatures with an electron beam, and using a stripping solution to eliminate undeveloped photoresist, thus removing excess metal.

The electrical characteristics of NbIrTe_4 were evaluated with a Keythley4200A semiconductor parameter tester. At room temperature electrodes were connected at both ends using a probe station and voltage was applied to measure the current flowing through the device. The resulting I - V curve depicted in Figure 5b is nearly a straight line through the origin, indicating effective ohmic contact. Figures 5c and 5d show the photoresponse of the NbIrTe_4 detector at 0 V and 0.01 V bias with a terahertz power density of 0.51969 mW/cm² respectively. At zero bias, the device exhibits a responsivity of 1.38 A/W and a noise equivalent power of approximately 4.65 pW/Hz^{1/2} indicating its capability for self-driving with mini-

mal energy thus enabling ultra-sensitive photodetection and ultra-low power devices. The device demonstrates a strong photoresponse at zero bias and when a bias is applied, the photocurrent increases further. At a bias of 0.01 V, the responsivity rises to 4.36 A/W, with a noise equivalent power of 12.34 pW/Hz^{1/2}. The responsivity is calculated based on the photocurrent, terahertz power density and the effective area of the device.

Noise Equivalent Power (NEP) is calculated using

$$NEP = \frac{V_n}{R_A} = \frac{\sqrt{(4k_b T/r + 2qI_d)}}{R_A}, \quad (1)$$

where R_A is the current response rate, k_b is the Boltzmann constant, T is the Kelvin temperature, r is the resistance, q is the elementary charge and I_d is the bias current. V_n is the noise current rms, which is mainly thermal Johnson-Nyquist noise (V_t) and noise caused by bias current (V_b). Figure 5e clearly illustrates that within a specific range the laser power and terahertz power density exhibit a positive linear correlation. After being ex-

posed to air for a month, the $I-V$ curve was re-evaluated showing that the device remained stable with negligible changes in resistance, as illustrated in Figure 5f. The terahertz photoelectric response detection system consists of a femtosecond laser, a semiconductor parameter tester, a BNA crystal, a probe station and a 3D displacement stage, as illustrated in Figure 5g. During measurements the terahertz source is a polychromatic light with 1 THz spectrum width generated by irradiating the BNA (N-benzyl-2-methyl-4-nitroanilin) organic crystal with an 800 nm femtosecond laser, with power calibrated using the THZ-B-DZ series terahertz power meter from Gentec-EO^[31].

To investigate the material's anisotropy, we constructed an eight-electrode setup with each electrode positioned 45 degrees apart, as depicted in Figure 6a. The average ratio of the maximum resistance to the minimum resistance (R_{\max}/R_{\min}) was calculated to be 32 as shown in Figure 6b. This observed anisotropy is linked to the low symmetry of the NbIrTe_4 crystal structure particularly with the x -axis being significantly smaller than the y -ax-

is. Figure 6c compares the performance of detectors made from various materials and Table 1 provides detailed data. The red five-pointed star indicates our device, which clearly shows advantages in responsiveness and noise equivalent power further highlighting the significant potential of Weyl semimetal materials for terahertz detection.

When exposed to low-energy terahertz light (in the meV range), typical semiconductor materials struggle to produce significant photocurrent via the photovoltaic or photoconductivity effects. In contrast, the semi-metal NbIrTe_4 is capable of generating a substantial photocurrent even without any applied bias. We attribute this response primarily to the intra-band transition process and we have ruled out the possibility of the photothermoelectric effect due to the symmetrical design of the antenna.

As a representative example of a type-II Weyl semimetal, NbIrTe_4 exhibits an in vitro Weyl cone resulting from the breaking of inversion symmetry alongside topologically protected surface states. As illustrated in Figure 6d, the pronounced interaction between the tilted Weyl

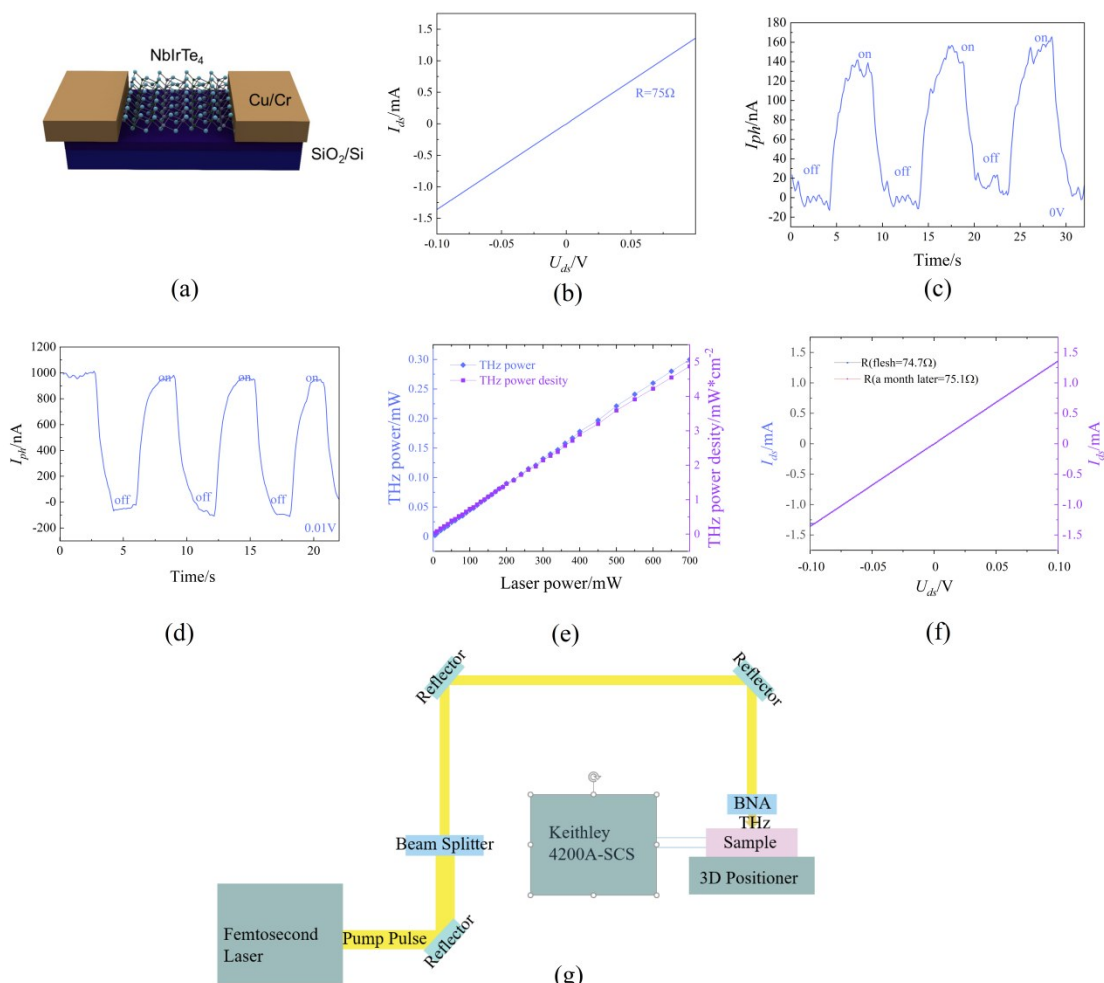


Fig. 5 Device measurement results: (a) Schematic diagram of the detector. (b) Electrical characteristics of the device. (c), (d) Terahertz response of the device under 0 bias and 0.01V bias. (e) Relationship between terahertz power and laser power. (f) The resistance change of the device after oxidation in air for one month. (g) Schematic diagram of terahertz photoelectric response test.

图5 器件的测量结果:(a)探测器的示意图;(b)器件的电学特性;(c),(d)器件在0偏压和0.01V偏压下的太赫兹响应;(e)太赫兹功率和激光功率关系;(f)器件在空气中氧化1个月的电阻变化;(g)太赫兹光电响应测试系统

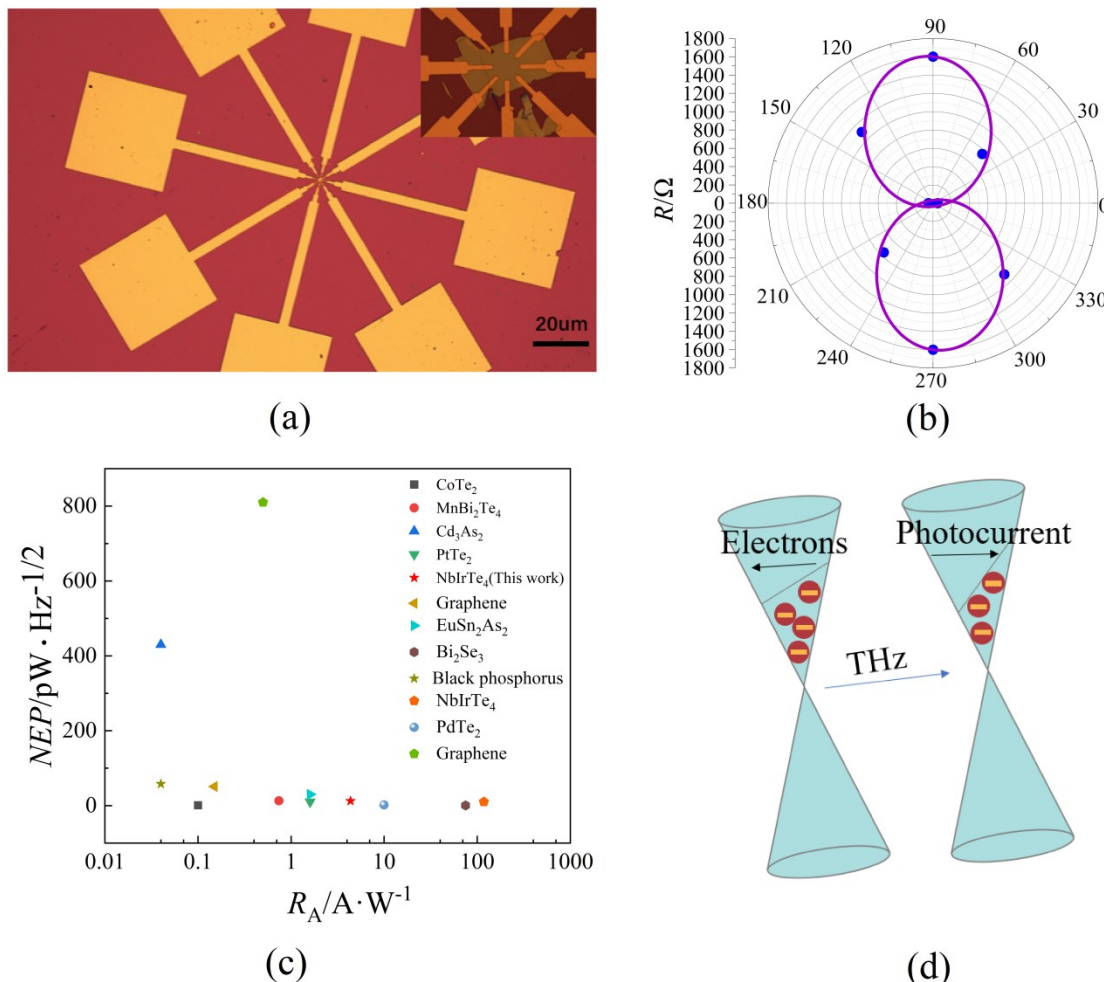


Fig. 6 Anisotropy of the device. (a) Designed eight electrodes, the inset is an enlarged view of the intersection of the electrode and the material. (b) Resistance values measured at every 45-degree angle, the maximum resistance ratio reaches 32. (c) Comparison of responsivity and noise equivalent power with other detectors. The abscissa is displayed using log10 logarithmic coordinates. (d) Schematic diagram of photocurrent generation of NbIrTe₄.

图6 器件的各向异性。(a) 设计的八电极, 插图是电极和材料交点的放大图。(b) 每隔45度角测量的电阻值, 最大电阻比达到32。(c) 和其他探测器的响应度和噪声等效功率的比较。横坐标使用了log10对数坐标显示。(d) NbIrTe₄的光电流产生示意图。

Table 1 Performance Comparison of the Reported 2D Materials Terahertz Detectors at Room Temperature

表1 已报道的二维材料太赫兹探测器在室温下的性能

Materials	THz	$R_A/A \cdot W^{-1}$	$NEP/pW \cdot Hz^{-1/2}$
NbIrTe ₄ (This work)	0.3	4.36	12.34
CoTe ₂ ^[32]	0.3	0.1	1
PtTe ₂ ^[33]	0.12	1.6	10
PdTe ₂ ^[34]	0.12	10	2
MnBi ₂ Te ₄ ^[35]	0.275	0.74	13
NbIrTe ₄ ^[36]	0.1	117.99	10
Bi ₂ Te ₃ ^[37]	0.022	2000	0.0075
Bi ₂ Se ₃ ^[38]	0.12	75	0.36
Cd ₃ As ₂ ^[39]	0.3	0.04	430
EuSn ₂ As ₂ ^[40]	0.3	1.6	30
Graphene ^[41]	0.33	0.15	51
Black Phosphorus ^[42]	0.12	0.04	58

cone of the semi-metallic NbIrTe₄ and terahertz waves leads to the breaking of inversion symmetry by spin-momentum-locked surface charge carriers, which in turn induces asymmetric oblique scattering. This phenomenon results in external excitations characterized by varying chirality. The non-equilibrium charge carriers at the Er point are elevated to higher energy states, prompting alterations in the charge distribution function. The presence of an electromagnetic field near the electrode combined with the broken inversion symmetry facilitates the escape of a limited number of charge carriers from the metal-material interface, thereby generating a non-zero photocurrent^[43-46]. Upon the application of a bias voltage to the device, the non-equilibrium carriers, which are generated by the strong local field produced by the oscillating electromagnetic field are accelerated and directed along the channel leading to a significant enhancement of the photocurrent.

3 Conclusion

This study employs first-principles calculations to derive the energy band structure and surface states of NbIrTe_4 . It utilizes mechanical exfoliation to fabricate layered materials of NbIrTe_4 , subsequently developing NbIrTe_4 -based field-effect transistors through micro-nano processing techniques and evaluates the electrical properties of the device. The terahertz photoelectric responses were systematically tested and analyzed. The findings indicate that the detector based on the Weyl semimetal NbIrTe_4 exhibits a pronounced optical response to terahertz radiation, achieving a responsivity of 4.36 A/W and an equivalent noise power of approximately 12.34 pW/Hz^{1/2}. Notably, the device maintains a terahertz response of 1.38 A/W even in the absence of bias. The results of this research suggest that the NbIrTe_4 terahertz photodetector holds significant potential for applications in terahertz detection and photoelectric signal conversion.

References

- [1] WU Jing-Zhu, YUAN Xi-Yan, YANG Yi, et al. Research on terahertz image analysis of thin-shell seeds based on semantic segmentation [J]. *Spectrochimica Acta Part A: Molecular and Biomolecular Spectroscopy*, 2024, 323: 124897.
- [2] CHEN Meng-Qi, LI Ya-Hui, WANG Bin*, et al. High-efficiency self-powered broadband photodetector based on $\text{PtSe}_2/\text{MoSe}_2$ heterojunction [J]. *ACS Photonics*, 2024, 11(4): 1693–1702.
- [3] ZUO Xin-Rong, ZHU Chen-Wei, YAO Chen-yu, et al. High sensitivity HgTe room temperature terahertz photodetector [J]. *APL Photonics*, 2023, 8(4).
- [4] GUO Yuan-Shen, CHEN Li-Gang, YAN Shi-Han, et al. Current research status of terahertz biomedical applications [J]. *Journal of Infrared and Millimeter Waves*, 2024, 43(5): 642–656. (郭缘森, 陈利刚, 颜识涵, 等. 太赫兹生物医学应用研究现状 [J]. 红外和毫米波学报), 2024, 43(5): 642–656.
- [5] YU Zi-Hao, LIN Hai, ZHOU Rui, et al. A high-Q topological refractive index sensor based on high-order corner states [J]. *Optics & Laser Technology*, 2025, 181: 111582.
- [6] GAO Xiang-Quan, LI Sheng-Hong, HE Ya-Kai, et al. Spectrum imaging for phenotypic detection of greenhouse vegetables: A review [J]. *Computers and Electronics in Agriculture*, 2024, 225: 109346.
- [7] ZHANG Min, CHEN Run, SONG Qi, et al. Polarization-resolved ultrafast all-optical terahertz micro-grating array modulator based on Weyl semimetallic microfilm towards 6G technology [J]. *Results in Physics*, 2023, 47: 106342.
- [8] SHI Jia, LUO Yue-Ping, WANG Shao-Na, et al. Artificial intelligence-assisted accurate spectrum prediction in design of terahertz fiber operating in 6G communication window [J]. *IEEE Journal of Selected Topics in Quantum Electronics*, 2023, 30(6): 8500108.
- [9] WEN Shu-Qing, ZHANG Wei-Rong, SUN Yi-Fu, et al. An enhanced principal component analysis method with Savitzky – Golay filter and clustering algorithm for sensor fault detection and diagnosis [J]. *Applied Energy*, 2023, 337: 120862.
- [10] LIU Xiao-Nan, QIAO Shun-Da, MA Yu-Fei. Highly sensitive methane detection based on light-induced thermoelastic spectroscopy with a 2.33 μm diode laser and adaptive Savitzky–Golay filtering [J]. *Optics Express*, 2022, 30(2): 1304–1313.
- [11] SI Jia-Shun, XIAO Xue-Feng, ZHANG Yan, et al. Pyroelectric properties and applications of Lithium Tantalate crystals [J]. *Crystals*, 2024, 14(7): 579.
- [12] ODON A, SZLACHTA A. Voltage response of a pyroelectric detector to a single rectangular optical radiation pulse [J]. *Sensors*, 2022, 22(16): 6265.
- [13] MOROHASHI I, IRIMAJIRI Y, KAWAKAMI A, et al. Wireless signal transmission at the 2 and 3 THz-Band enabled by photonics-based transmitter and hot electron bolometer mixer [J]. *IEEE Journal of Selected Topics in Quantum Electronics*, 2023, 29(5): 1–7.
- [14] RYZHII V, TANG C, OTSUJI T, et al. Effect of electron thermal conductivity on resonant plasmonic detection in terahertz hot-electron bolometers based on metal/Black-AsP/graphene FETs [J]. *Physical Review Applied*, 2023, 19(6): 064033.
- [15] NANDI S, MISRA A. Carbon nanotube-based uncooled bolometers: advances and progress [J]. *ACS Materials Letters*, 2022, 5(1): 249–274.
- [16] MARCON R, KAUFMANN P, FERNANDES L O T, et al. Terahertz photometer to observe solar flares in continuum [J]. *Journal of Infrared, Millimeter, and Terahertz Waves*, 2012, 33: 192–205.
- [17] PASCHOS G G, LIEW T C H, HATZOPOUIOS Z, et al. An exciton–polariton bolometer for terahertz radiation detection [J]. *Scientific Reports*, 2018, 8(1): 10092.
- [18] LIU Pu, CUI Chao-Xi, LI Xiao-Ping, et al. Landau level spectrum and magneto-optical conductivity in tilted Weyl semimetal [J]. *Physical Review B*, 2023, 107(8): 085146.
- [19] LIU Jing, XIA Feng-Nian, XIAO Di, et al. Semimetals for high-performance photodetection [J]. *Nature materials*, 2020, 19(8): 830–837.
- [20] MA Jun-Chao, GU Qiang-Qiang, LIU Yi-Nan, et al. Nonlinear photoresponse of type-II Weyl semimetals [J]. *Nature materials*, 2019, 18(5): 476–481.
- [21] ZHOU Wei, LI Bin, XU Chun-Qiang, et al. Nonsaturating magnetoresistance and nontrivial band topology of type-II Weyl semimetal NbIrTe_4 [J]. *Advanced Electronic Materials*, 2019, 5(8): 1900250.
- [22] KUMAR D, HSU C H, SHARMA R, et al. Room-temperature nonlinear Hall effect and wireless radiofrequency rectification in Weyl semimetal TaIrTe_4 [J]. *Nature Nanotechnology*, 2021, 16(4): 421–425.
- [23] ZHU Zing-Ming, YU Zhi-Ming, WU Wei-Kang, et al. Composite Dirac semimetals [J]. *Physical Review B*, 2019, 100(16): 161401.
- [24] FANG Chen, WENG Hong-Ming, DAI Xi, et al. Topological nodal line semimetals [J]. *Chinese Physics B*, 2016, 25(11): 117106.
- [25] ZHU Ye, ZHAO Bao, XUE Yang, et al. From topological nodal-line semimetals to quantum spin Hall insulators in tetragonal SnX monolayers ($\text{X} = \text{F}, \text{Cl}, \text{Br}, \text{I}$) [J]. *Chinese Physics Letters*, 2024, 41(6): 067301.
- [26] XU S Y, ALIDOUST N, BELOPOLSKI I, et al. Discovery of a Weyl fermion state with Fermi arcs in niobium arsenide [J]. *Nature Physics*, 2015, 11(9): 748–754.
- [27] XU S Y, BELOPOLSKI I, SANCHEZ D S, et al. Experimental discovery of a topological Weyl semimetal state in TaP [J]. *Science advances*, 2015, 1(10): e1501092.
- [28] LAI, Jia-Wei, MA Jun-Chao, Fan Zi-Pu, et al. Direct light orbital angular momentum detection in mid-infrared based on the type-II Weyl semimetal TaIrTe_4 [J]. *Advanced Materials*, 2022, 34(29).
- [29] EKAHANA S A, LI Y W, SUN Y, et al. Topological Lifshitz transition of the intersurface Fermi–arc loop in NbIrTe_4 [J]. *Physical Review B*, 2020, 102(8): 085126.
- [30] YU N, WANG Q J, KATS M A, et al. Designer spoof surface plasmon structures collimate terahertz laser beams [J]. *Nature materials*, 2010, 9(9): 730–735.
- [31] ZHAO Hang, WU Tong, TAN Yong, et al. Efficient broadband terahertz generation from organic crystal BNA using near infrared pump [J]. *Applied Physics Letters*, 2019, 114(24).
- [32] HU Zhen, ZHANG Li-Bo, CHAKRABORTY A, et al. Terahertz nonlinear Hall rectifiers based on spin polarized topological electronic states in 1T-CoTe_2 [J]. *Advanced Materials*, 2023, 35(10): 2370071.
- [33] XU Huang, GUO Cheng, ZHANG Jia-Zhen, et al. PtTe_2 -based type-II Dirac semimetal and its van der Waals heterostructure for sensitive room temperature terahertz photodetection [J]. *Small*, 2019, 15(52): 1903362.
- [34] GUO Cheng, HU Yi-Bin, CHEN Gang, et al. Anisotropic ultrasensitive PdTe_2 -based phototransistor for room-temperature long-wavelength detection [J]. *Science Advances*, 2020, 6, eabb6500.
- [35] GUO Cheng, CHEN Z Q Z, YU Xian-Bin*, et al. Ultrasensitive anisotropic room-temperature terahertz photodetector based on an intrinsic magnetic topological insulator MnBi_2Te_4 [J]. *Nano Letters*, 2022, 22(18): 7492–7498.
- [36] ZHANG Jian-Tian, ZHANG Tian-Ning, YAN Luo, et al. Colossal room-temperature terahertz topological response in type-II Weyl semimetal NbIrTe_4 [J]. *Advanced Materials*, 2022, 34, 2204621.
- [37] XU Xin-Yue, ZHANG Xiao-Dong, WU Jing, et al. High responsivity Bi_2Te_3 -based room-temperature terahertz detector based on metal-semiconductor-metal (MSM) structure [J]. *Journal of Infrared*

- Millimeter Waves, 2019, 38(4):459–463.
(徐新月, 张晓东, 吴敬等. 基于金属-半导体-金属结构的 Bi_2Te_3 室温高响应率太赫兹探测器[J]. 红外与毫米波学报), 2019, 38(4):459~463.
- [38] TANG Wei-Wei, POLITANO A, GUO Cheng, et al. Ultrasensitive room-temperature terahertz direct detection based on a bismuth selenide topological insulator [J]. Advanced Functional Materials [J]. 2018, 28, 1801786.
- [39] YAO Xiao-Mei, ZHANG Sheng-Xi, SUN Qiang, et al. Thickness-controlled three-dimensional Dirac semimetal for scalable high-performance terahertz optoelectronics [J]. ACS Photonics, 2021, 8(6): 1689–1697.
- [40] LIU Chang-Long, LIU Yi, CHEN Z Q Z, et al. A candidate material EuSn_2As_2 -based terahertz direct detection and imaging [J]. npj 2D Materials and Applications, 2022, 6, 26.
- [41] QIN Hua, SUN Jia-Dong, LIANG Shi-xiong, et al. Room-temperature, low-impedance and high-sensitivity terahertz direct detector based on bilayer graphene field-effect transistor [J]. Carbon, 2017, 116: 760–765.
- [42] GUO Wang-Long, DONG Zhuo, XU Yi-Jun, et al. Sensitive terahertz detection and imaging driven by the photothermoelectric effect in ultrashort-channel black phosphorus devices [J]. Advanced Science, 2020, 7, 1902699.
- [43] CHAN C K, LINDNER N H, REFAEL G, et al. Photocurrents in Weyl semimetals [J]. Physical Review B, 2017, 95(4): 041104.
- [44] HUANG Li, TAN Wee-Chong, WANG Lin, et al. Infrared black phosphorus phototransistor with tunable responsivity and low noise equivalent power [J]. ACS applied materials & interfaces, 2017, 9(41): 36130–36136.
- [45] VITI L, POLITANO A, VITIELLO M S. Black phosphorus nanodevices at terahertz frequencies: Photodetectors and future challenges [J]. APL Materials, 2017, 5(3): 035602.
- [46] HE Yuan, YANG Liu, HU Zhen, et al. Selective growth of type-II Weyl semimetal and van der Waals stacking for sensitive terahertz photodetection [J]. Advanced Functional Materials, 2024, 34(12): 2311008.